Full Length Article

Single-atom iron as a promising low-temperature catalyst for selective catalytic reduction of NO$_x$ with NH$_3$: A theoretical prediction

Weijie Yang [a], Jianuo Ren [a], Hanwen Zhang [a], Jiajia Li [a], Chongchong Wu [b], Ian D. Gates [b], Zhengyang Gao [a],*

[a] School of Energy and Power Engineering, North China Electric Power University, Baoding 071003, China
[b] Department of Chemical and Petroleum Engineering, University of Calgary, T2N 1N4 Calgary, Alberta, Canada

ARTICLE INFO

ABSTRACT

Selective catalytic reduction of NO$_x$ with NH$_3$ (NH$_3$-SCR) is a dominant technology to reduce NO$_x$ (deNO$_x$). However, there are two shortcomings for commercial deNO$_x$ catalysts (vanadium-titanium-based metal oxides), such as poor low-temperature efficiency and toxicity. Thus, it is urgent to develop environmentally friendly low-temperature catalysts with high deNO$_x$ efficiency. Therefore, we firstly proposed a single-atom iron coordinated with four N atoms (Fe$_1$-N$_4$) as a novel low-temperature NH$_3$-SCR catalyst, due to its high coordination unsaturation and safety. The detailed reaction mechanisms are revealed via density functional theory calculations and microkinetic modeling. Seven possible reaction pathways were found in the NH$_3$-SCR reaction. Different from metal oxides, special intermediates such as N$_2$H and NHNO are found in the reaction pathway. The dominant pathway of the NH$_3$-SCR reaction over the Fe$_1$-N$_4$ catalyst is a three-step process including NO oxidation, NO$_2$ reduction, and NHNO decomposition. The suitable temperature window of the Fe$_1$-N$_4$ catalyst is <430 K due to its relatively low energy barrier of 0.99 eV. Different from other metal oxide catalysts, the fast oxidation of NO on Fe$_1$-N$_4$ catalyst significantly promotes the reaction rate of NH$_3$-SCR on Fe$_1$-N$_4$ catalyst. Based on its outstanding performance, we believe that single Fe atom catalyst can provide new insights to design novel catalysts for NH$_3$-SCR.

1. Introduction

Nitrogen oxides (NO$_x$) from fossil fuel combustion are considered as a key contributor to anthropogenic emissions since it leads to environmental problems such as acid rain, photochemical smog, greenhouse effect and smog [1]. Currently, several deNO$_x$ technologies have been developed including selective catalytic reduction (SCR), selective non-catalytic reduction (SNCR), and nonselective catalytic reduction (NSCR) [2]. SCR processes using NH$_3$ as a reducing agent have been industrially applied in combustion units due to a higher NO$_x$ removal efficiency than that of SNCR or combustion control [3].

Commercial catalysts for NH$_3$-SCR are mainly vanadium-titanium-based metal oxides, such as V$_2$O$_5$-WO$_3$/TiO$_2$ and V$_2$O$_5$-MoO$_3$/TiO$_2$, etc. [4]. The NO$_x$ conversion rate can reach more than 90% within its operation temperature window (300–400 °C). Due to its narrow and high operating temperature window, SCR devices are permanently placed between the economizer and air preheater in coal-fired power

plants [5,6]. Simultaneously, due to the renewable energy synchronization, low-load operation of power plants has become the new trend. When the load of 300 MW units is dropped to 35%, the temperature of the flue gas at the entrance of the SCR devices is ~275 °C [7,8]. However, the low-temperature (<300 °C) catalytic activity of vanadium-titanium-based catalysts is low, resulting in a significant reduction in the NO$_x$ conversion rate and making it difficult to meet NO$_x$ pollutant emission standards [9]. In addition, the waste V-based metal oxide catalysts are highly toxic to the environment. Therefore, environmentally friendly low-temperature catalysts are being sought for control of NO$_x$ pollution in coal-fired power plants.

The NH$_3$-SCR reaction mainly consists of the "standard SCR" (4NH$_3$ + 4NO + O$_2$ → 4 N$_2$ + 6H$_2$O) and "Fast SCR" (2NH$_3$ + NO + NO$_2$ → 2 N$_2$ + 3H$_2$O) pathways. The reaction rate of the latter is 10 times faster than that of the former at low temperature [10], indicating that the addition of NO$_2$ can significantly increase the reaction rate of NH$_3$-SCR at low temperature. Therefore, catalytic oxidation of a part of the NO in the flue

* Corresponding author.
E-mail address: gaozhyan@163.com (Z. Gao).

gas to NO_2 is beneficial to promote the "Fast SCR" reaction, and ultimately improve the deNO$_x$ efficiency of the metal oxide catalysts. However, the surface of metal oxide catalysts is coordination saturated, resulting in poor adsorption and activation capacity for the O_2 molecule; as a result, the NO oxidation rate of metal oxide catalysts is generally lower than 40% at 200 °C [11]. In recent years, Mn-based [12], Fe-based [13], Cu-based [14], and Ce-based [15] low-temperature metal oxide catalysts have been studied. By creating vacancy defects and doping metal ions on the surface of the metal oxides [16], the surface coordination is unsaturated and its low-temperature catalytic activity is enhanced. These metal oxide catalysts realize the catalytic reduction of NO at lower temperatures nearer 200 °C, but the NO conversion rate of most catalysts is less than 80%. When evaluated against existing emission standards, the low-temperature catalytic activity of current metal oxides is obviously insufficient.

Considering the high coordination unsaturation of single-atom catalysts (SACs), we infer that SACs have potential advantages in the NH$_3$-SCR reaction. Although there have been few studies on the use of SACs in the NH$_3$-SCR reaction so far, the high catalytic activity of SACs at low temperature has been proved by previous research [17]. Zhang et al. [18] used H_2 as a reducing agent to carry out a low-temperature catalytic activity experiment for the reduction of NO over single-atom Pd catalyst; they showed 100% conversion rate of NO could be achieved at 200 °C. On the other hand, Furukawa et al. [19] used CO as a reducing agent, and the conversion rate of NO could reach 100% at 175 °C. The studies by Deng et al. indicated that the single-atom Fe catalyst could achieve the catalytic oxidation of benzene [20] and methane [21] at room temperature. In addition, the Fe$_1$-N$_4$ catalyst can be synthesized through high-temperature pyrolysis and strong acid etching [22], suggesting that Fe$_1$-N$_4$ catalyst should have high thermal stability and strong acid resistance, which is critical for its engineering application in coal-fired power plant.

Our previous researches show that the single-atom iron catalyst (Fe$_1$-N$_4$) has good O_2 activation ability [23] and NO oxidation ability [24], so we infer that the Fe$_1$-N$_4$ can carry out the NH$_3$-SCR reaction. A single iron atom serves as the catalytic active center and its coordination is highly unsaturated. Unpaired electrons of the d orbital give it favorable redox ability, which is beneficial for the activation of the O_2 molecule at low temperature promoting the "Fast SCR" reaction [25]. Simultaneously, the Fe$_1$-N$_4$ catalyst is environmentally friendly and inexpensive given the abundance of Fe, which makes it suitable for engineering applications.

To explore the feasibility of NH$_3$-SCR reaction on Fe$_1$-N$_4$ in detail, we first considered the possible adsorption structures of various gases (NH$_3$, NO, NO$_2$, O$_2$, ·OH, N$_2$) on Fe$_1$-N$_4$ to lay the foundation for reaction path analysis. Secondly, based on the adsorption sequence, the reaction pathways of NH$_3$-SCR over Fe$_1$-N$_4$ catalyst were systematically studied. Additionally, thermodynamic analysis and kinetic analysis were carried out to determine the influence of temperature on the equilibrium constant (K) and reaction rate constant (k^{TST}). Finally, microkinetics modeling was performed to calculate the turnover frequency (TOF) of the NH$_3$-SCR reaction and the coverage of surface species. The rate-determining step (RDS) of the whole reaction and the influence of temperature and pressure on reaction rate were discussed. This theoretical research can provide a new perspective for the design of NH$_3$-SCR catalysts.

2. Method

Considering that density functional theory (DFT) calculation has the advantages of being efficient and accurate with an energy accuracy of 2–3 kcal/mol [26], a systematic DFT calculation was carried out to quickly verify the catalytic activity of the Fe$_1$-N$_4$ catalyst in NH$_3$-SCR reaction. All calculations were performed by the Vienna ab initio simulation package software (VASP 5.4.4) [27,28]. To be specific, the Projector-Augmented-Wave (PAW) method was adopted to characterize the interaction between the nucleus and valence electrons, and the Perdew-Burke-Ernzerhof (PBE) method was used to describe the exchange and correlation energy of electrons [29]. Considering the low loading of graphene in the experiment and the periodic mirror effect, a 5x5 single-layer graphene with a 15 Å vacuum layer was selected as the substrate. To obtain the accurate lattice constant of the graphene model, the lattice constant of the graphene model has been automatically optimized through setting ISIF = 3. Based on our test (shown in Fig. S1), a $4 \times 4 \times 1$ Γ-centered K-point grid was used for geometric optimization [30]. Our previous studies have shown that a 450 eV energy cutoff and 0.02 eV/Å force convergence standard are suitable to acquire accurate results [31–33]. The self-consistent total energy calculation used a more intensive $8 \times 8 \times 1$ K-point grid with 10^{-5} eV self-consistent electron iteration as the convergence threshold. Given the unpaired d electrons of Fe atom, the spin polarization (ISPIN) was set equal to 2 [34,35]. To get more accurate optimized structures and calculate adsorption energy more precisely, especially for NH$_3$, Van der Waals interaction was included by using the DFT-D3 correction [36].

To acquire the accurate transition states, the climbing-image nudged elastic band (CI-NEB) method [37–39] was selected to roughly obtain the general reaction paths and transition states. Moreover, the improved dimer method (IDM) [40] was applied to accurately locate the transition states derived from the results calculated by CI-NEB method. This joint strategy with the force convergence tolerance of 0.05 eV/Å has been proved to be an effective method for quickly locating the transition states by our previous studies [24,41]. The accuracy of transition states and system energy was calculated by vibrational frequency, which was operated under limited displacements of ±0.02 Å [42,43].

The energy of the gas adsorbed on single-atom iron catalysts was expressed by the adsorption energy (E_{ads}) which measures the adsorption strength of the adsorbent and adsorbate as follows:

$$E_{ads} = E_{tot} − E_{sur+Fe} − E_{gas} \quad (1)$$

where E_{tot}, E_{sur+Fe} and E_{gas} represent the total energy of the adsorption system, substrate and gases respectively. The more negative the adsorption energy, the more stable is the adsorption.

The reaction energy barrier (E_b) and heat (ΔE) in the reaction paths were expressed by the following two formulas:

$$E_b = E_{TS} − E_{IS} \quad (2)$$

$$\Delta E = E_{FS} − E_{IS} \quad (3)$$

where E_{IS}, E_{TS} and E_{FS} represent the energy of the initial state, transition state, and final state, respectively.

The equilibrium constant (K) was calculated to perform thermodynamic analysis as follows [44]:

$$\Delta G = G_{FS} − G_{IS} = -RT·\ln K \quad (4)$$

where G_{IS} and G_{FS} are Gibbs free energy of initial and final state; R is the universal gas constant; T is the temperature, and K is the equilibrium constant.

To be specific, the calculation of Gibbs free energy could be divided into the gas and solid categories [45]:

$$G_{gas}(T) = E_{ele} + ZPE + RT − TS \quad (5)$$

$$G_{solid}(T) = E_{ele} + ZPE − TS \quad (6)$$

where E_{ele} is the system energy in ground state; ZPE is the zero correction energy; T is the temperature; and S is the entropy of whole system acquired from vibrational frequency.

The reaction rate constant (k^{TST}) was calculated to perform kinetic analysis in the light of the classical transition state theory as follows [44]:

$$k^{TST} = \frac{k_B T}{h} \times exp\left(\frac{-\Delta G_b}{k_B T}\right) \quad (7)$$

where k_B is the Boltzmann constant, 8.6173303 $\times 10^{-5}$ eV·K^{-1}; h is the Planck constant, 6.582119514 $\times 10^{-16}$ eV·s; ΔG_b is the energy barrier in Gibbs free energy, eV.

3. Results and discussion

3.1. Catalyst model

The optimized lattice constant and bond length are 2.46 Å and 1.42 Å, respectively, which are consistent with the experimental value and theoretical data [46]. The geometric structure of Fe_1-N_4 catalyst is shown in Fig. 1(a). In this theoretical calculation model, the active site is Fe atom coordinated with four N atoms, corresponding to the Fe K-edge Fourier transform-extended X-ray absorption fine structure (FT-EXAFS) spectrum in the previous experiment research [22,47,48]. The Fe loading rate is 8.7 wt%, which is similar to the previous experimental study (8.9 wt%) [49]. Based on the above analysis, this theoretical calculation model of Fe_1-N_4 catalyst should be reasonable. Considering that the stability of catalyst is critical for its application, the thermal stability and structural stability of Fe_1-N_4 catalyst were verified through binding energy and ab initio molecular dynamics (AIMD) simulation. The strong binding energy (-7.20 eV) is significantly larger than its cohesive energy (-4.28 eV) [50], indicating that the graphene-based substrate can firmly anchor Fe atoms. In addition, to further verify the structural stability of Fe_1-N_4 catalyst, an AIMD simulation at 900 K under 10 ps was performed to study the variation of energy and bond length. The system energy and bond length of Fe-N both fluctuate in a small range even at the high temperature of 900 K, indicating that Fe_1-N_4 catalyst should have high stability for the catalytic reaction of NH_3-SCR.

3.2. Gas adsorption

Given the complexity of the NH_3-SCR reaction, the adsorption energy of the main reaction gases, including NH_3, NO, NO_2 O_2 and H_2O, were calculated to lay the foundation for the subsequent reaction path search, as shown in Fig. 1(b). Similar to other metal oxide catalysts [51,52], the adsorption of NH_3 is relatively weak. The adsorption energies of NO, NO_2 and O_2 on the Fe_1-N_4 catalyst are -1.94, -1.29, and -0.81 eV, respectively, belonging to the chemical adsorption. Moreover, the

adsorption energy of N_2 is -0.30 eV, indicating that the desorption process of generated N_2 from the Fe_1-N_4 catalyst is relatively easy. In addition, the adsorption energy of H_2O is 0.18 eV, suggesting that the desorption process of the NH_3-SCR product should occur spontaneously.

3.3. Detailed reaction process

To explore the mechanism of NH_3-SCR reaction on the Fe_1-N_4 catalyst, we constructed possible reaction paths by tuning the adsorption order of reaction gases, including NH_3 adsorption, NO adsorption, NO_2 adsorption, and O_2 adsorption. Given that the generated ·OH, as an active radical, can take part in the NH_3-SCR reaction, the reaction path was also included in this work. All configurations of NH_3-SCR reaction in different reaction paths were plotted in Fig. 2. Correspondingly, expressions of different reaction paths were listed in Table1. The energy variation maps of corresponding reaction paths were plotted in Figs. S2 to S9.

3.3.1. NO adsorption

For path1 (as shown in Figs. 2 and S2), the NH_3 from the gas phase dissociates into NH_2 fragment and H atom. The resulting H atom migrates to an O atom and the N atom of NH_2 fragment interacts with the N atom of NO to form the intermediate (IM1). The energy barrier and heat of reaction are 2.54 eV and 1.66 eV, respectively. A positive heat of reaction indicates that the reaction is endothermic. The intermediate (IM1) is not strongly stable and continues to decompose to N_2H^* and H_2O. The reaction energy barrier of 0.34 eV reveals that the reaction is more likely to occur and the reaction releases a relatively large heat of reaction equal to -3.36 eV to promote the subsequent dehydrogenation of N_2H. In the reaction pathway of $N_2H^* \rightarrow N_2^* + H^*$, the H atom of the N_2H fragment is extracted by the C atom through the transition state (TS3). The dehydrogenation reaction is an endothermic reaction with an activation energy barrier of 1.07 eV and heat of reaction is 0.06 eV.

3.3.2. NH_3 adsorption
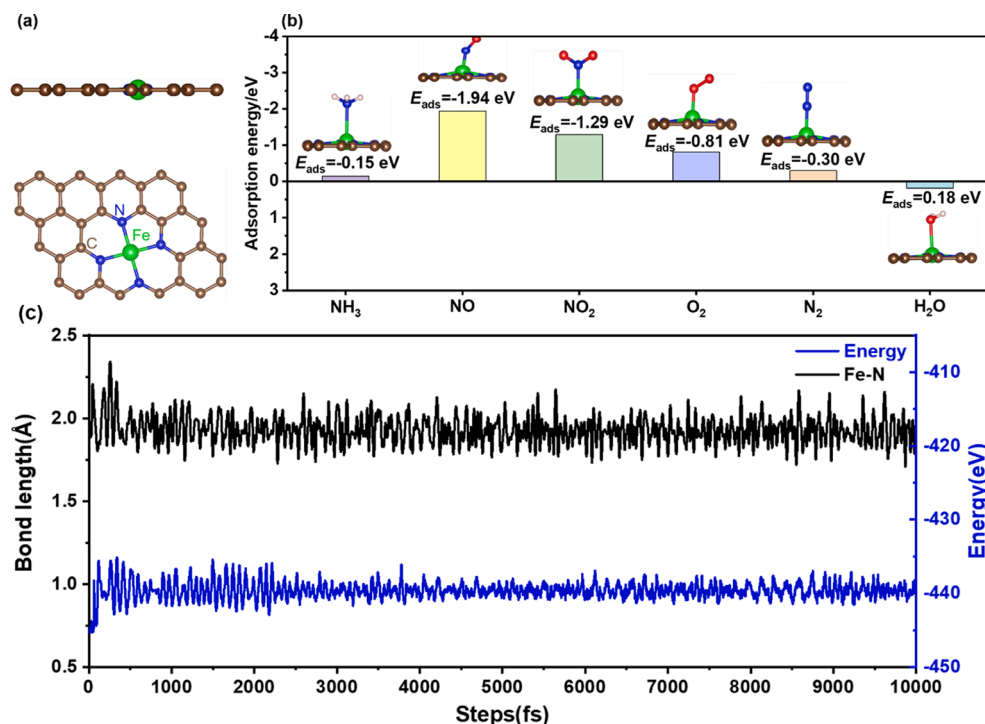
NH_3^* can undergo reduction reactions with NO, NO_2, or a

Fig. 1. (a) The geometric structure of Fe_1-N_4. (b) The most stable structures and adsorption energies of NH_3, NO, NO_2, O_2, N_2 and H_2O on Fe_1-N_4 catalyst. (c) Energy and bond length variation of Fe_1-N_4 catalyst in AIMD simulation at 900 K under 10 ps with a time interval of 1 fs.
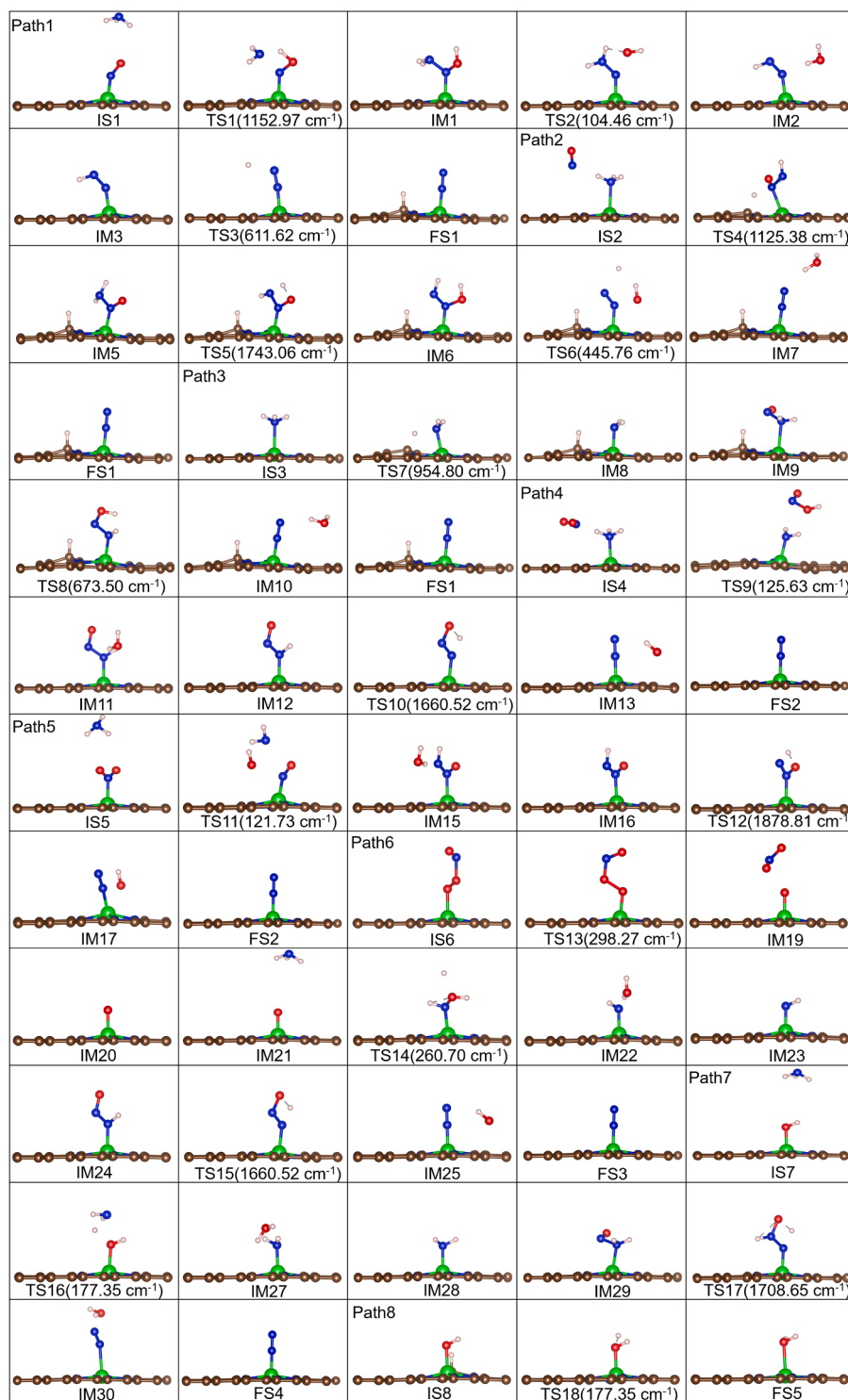
Fig. 2. The configurations of initial states, transition states, intermediates, and final states for NH_3-SCR.

dehydrogenation reaction. Different from path1, in path2 (as shown in Figs. 2 and S3), the NO molecule attacks the NH_3 molecule and causes the NH_3 molecule to decompose to NH_2 fragment and an H atom. The generated H atom is captured by a C atom to form a C–H bond, and the NH_2 fragment combines with the NO molecule to form the NH_2NO intermediate through a N-N coupling reaction. The NH_2NO intermediate has been confirmed to exist in Liu et al.'s [53] experiments and the reaction pathway agrees with that over the monomeric vanadia/TiO_2 surfaces [54]. The reaction needs to overcome a 1.72 eV energy barrier

and absorb 1.06 eV of heat. The energy barrier is slightly higher than that (1.36 eV) reported by He et al. [54]. Afterwards, the O atom strips an H atom from the NH_2 fragment to generate a new intermediate (IM6). The cleavage of the N–H bond and formation of the O–H bond are observed in this step. This step is an endothermic reaction with an activation energy barrier of 1.18 eV and heat of reaction being 0.42 eV. In the final decomposition step, IM6 decomposes to H_2O and N_2. The decomposition reaction is activated by 1.14 eV, and a relatively large heat (-2.70 eV) is released to promote the desorption of N_2.

Table 1
Complete reaction mechanism of NH_3-SCR on Fe_1-N_4 catalyst.

No.	Reaction	No.	Reaction
Part 1 NO adsorption pathway		5–1	$NH_3 + NO_2^* \rightarrow NHNO^* + H_2O$
1–1	$NH_3 + NO^* \rightarrow N_2H^* + H_2O$	5–2	$NHNO^* \rightarrow N_2^* + \cdot OH$
1–2	$N_2H^* \rightarrow N_2^* + H^*$	Part 4 O_2 adsorption pathway	
Part 2 NH_3 adsorption pathway		6–1	$NO + O_2^* \rightarrow O^* + NO_2$
2–1	$NO + NH_3^* \rightarrow NH_2NO^* + H^*$	6–2	$NH_3 + O^* \rightarrow NH^* + H_2O$
2–2	$NH_2NO^* \rightarrow N_2^* + H_2O$	6–3	$NHNO^* \rightarrow N_2^* + \cdot OH$
3–1	$NH_3^* \rightarrow NH_2^* + H^*$	Part 5 $\cdot OH$ adsorption pathway	
3–2	$NH_2NO^* \rightarrow N_2^* + H_2O$	7–2	$NH_3 + OH^* \rightarrow NH_2^* + H_2O$
4–1	$NO_2 + NH_3^* \rightarrow NHNO^* + H_2O$	7–3	$NH_2NO^* \rightarrow N_2^* + H_2O$
4–2	$NHNO^* \rightarrow N_2^* + \cdot OH$	Part 6 H removal pathway	
Part 3 NO_2 adsorption pathway		8–1	$OH^* + H^* \rightarrow H_2O^*$

In the NH_3 dehydrogenation step ($NH_3^* \rightarrow NH_2^* + H^*$), the NH_3 molecule dissociates into NH_2 fragment and H atom, as shown in Figs. 2 and S4. The N atom of the NH_2 fragment is coordinated with the Fe atom and the H atom transfers to a C atom. Due to the relatively weak activation of NH_3, the energy barrier of this step is 2.25 eV. The NH_2 fragment formed from NH_3 dehydrogenation reacts with the free NO spontaneously to generate NH_2NO species, which is consistent with the formation of the NH_2NO species over Mn-TiO_2 [55]. The process is exothermic with heat generated equal to −0.59 eV. Finally, the NH_2NO^* species decomposes to N_2 and H_2O through the transition state (TS8). The H atoms from the NH_2 fragment are stripped by the O atom in turn, and H_2O is generated. The decomposition reaction is an exothermic reaction with an energy barrier of 0.88 eV and heat of reaction −2.69 eV, which promotes subsequent N_2 desorption.

NO_2, as a reactant of the fast SCR reaction ($2NH_3 + NO + NO_2 \rightarrow 2 N_2 + 3H_2O$), can accelerate the reaction rate of NH_3-SCR. In the reaction pathway of $NO_2 + NH_3^* \rightarrow NHNO^* + H_2O$ (as shown in Figs. 2 and S5), the gas-phase NO_2 attacks the adsorbed NH_3 molecule. The cleavage of the N–H and N-O bonds is observed during the reaction. Finally, the reaction yields the $NHNO^*$ species and dissociative H_2O. The energy barrier and heat of reaction are 0.55 eV and −0.32 eV, respectively. Such a low energy barrier indicates that NO_2 molecule is more likely to undergo the reduction reaction with the NH_3 molecule. In the reaction pathway of $NHNO^* \rightarrow N_2^* + \cdot OH$, the NHNO species decomposes to form N_2 and $\cdot OH$ with an energy barrier of 0.99 eV and heat of reaction −0.39 eV.

3.3.3. NO_2 adsorption

For path5 (as shown in Figs. 2 and S6), the gas-phase NH_3 molecule attacks the NO_2 molecule, and two H atoms from NH_3 molecule are abstracted by the O atom from the NO_2 molecule to form H_2O. The resulting NH species interacts with produced NO molecule via a N-N coupling reaction to form the NHNO species. The reaction has a relatively high activation energy of 2.94 eV since the adsorption configuration of NO_2 on the catalyst surface is a stable configuration and the reaction heat is −0.15 eV. path4 and path5 are both reduction reactions of NO_2. However, the reaction energy barriers of path4 and path5 are different due to the distinct adsorption order, which is consistent with the conclusion drawn from the previous NO reduction reaction. In the elementary reaction step ($NHNO^* \rightarrow N_2^* + \cdot OH$), the NHNO species decomposes to form N_2 and $\cdot OH$. The decomposition reaction is an exothermic reaction with an energy barrier of 1.59 eV and heat of reaction being −0.29 eV.

3.3.4. O_2 adsorption

Based on our previous research [24], NO can be oxidized to NO_2 with a low energy barrier. NO_2 plays an important role in the fast SCR reaction. For path6 (as shown in Figs. 2 and S7), the NO molecule strips one of two O atoms to form gas-phase NO_2. The reaction just overcomes the 0.01 eV energy barrier and releases 0.56 eV heat, which indicates that NO is easily oxidized to NO_2 under the activity of the catalyst.

Afterwards, the resulting O^* atom continues to react with NH_3 and two H atoms from NH_3 molecule are extracted by the O^* atom. The reaction has a relatively high activation energy of 3.46 eV since the adsorption energy of O atom is −4.50 eV, which indicates that the desorption of generated H_2O may be relatively hard for the reaction of O atom with NH_3. Moreover, the reaction is an endothermic reaction with reaction heat of 0.41 eV. The produced NH fragment reacts with the NO molecule spontaneously to generate the NHNO species. The process releases a huge reaction heat of −2.04 eV to promote the decomposition of NHNO. Finally, the NHNO species dissociates into N_2^* and $\cdot OH$. The energy barrier and reaction heat are 0.99 eV and −0.38 eV, respectively.

3.3.5. $\cdot OH$ adsorption

Given that $\cdot OH$ originated from the above reaction paths may be involved in the NH_3-SCR reaction, its possible reaction path was also explored. For path7 (as shown in Figs. 2 and S8), the gas-phase NH_3 molecule attacks OH^* and decomposes to NH_2 fragment and H atom. The resulting H atom combines with $\cdot OH$ to generate H_2O. Desorption of the H_2O molecule and adsorption of the NH_2 fragment are also observed during the reaction. The reaction is an endothermic reaction with a high energy barrier of 4.52 eV and reaction heat of 0.10 eV. The generated NH_2 fragment can still react with NO spontaneously to form NH_2NO species and emit heat of −0.24 eV. In the reaction pathway of $NH_2NO^* \rightarrow N_2^* + H_2O$, the NH_2NO species finally decomposes to N_2^* and H_2O. The decomposition reaction only needs to overcome 0.85 eV to proceed and releases a lot of heat (-2.71 eV).

3.3.6. Removal of residual H atom

To complete the catalytic cycle of Fe_1-N_4 catalyst, the H atom generated in path1 to path3 should interact with $\cdot OH$ generated in path4 to path6. As shown in Figs. 2 and S9, the $\cdot OH$ first adsorbs on the Fe_1-N_4 site, and the cleavage of C–H bond and formation of H_2O molecule are observed via the transition state (TS16). The adsorption energy of H_2O is positive (0.18 eV), indicating that the H_2O molecule can directly desorb. The reaction is an exothermic reaction with an energy barrier of 1.19 eV and reaction heat of −1.42 eV.

3.3.7. Dominant reaction path analysis

To intuitively describe the energy variation of different pathways, the skeletal reaction scheme is illustrated in Fig. 3. The pathways to generate N_2 from the NH_3-SCR reaction over Fe_1-N_4 catalyst include seven different pathways. Compared with other reaction pathways, path4 exhibits lower energy barriers during the entire reaction process, which is conducive to the formation of N_2. Meanwhile, the desorption energy of N_2 is 0.48 eV in path1 to path3 (FS $\rightarrow$ P_1), and 0.3 eV in path4 to path7 (FS $\rightarrow$ P_2). Except for path1, the last steps of other paths are exothermic reactions. The huge release of heat is sufficient to make the N_2 desorb spontaneously at low temperatures. The NO molecule only needs to overcome 0.01 eV to generate a NO_2 molecule via NO + O_2^* $\rightarrow$ O^* + NO_2. Although the activation of NH_3 is insufficient on Fe_1-N_4, the super high catalytic activity of Fe_1-N_4 catalyst for NO oxidation significantly promotes the reaction rate of the NH_3-SCR reaction. Comparing the energy barriers of different pathways, we can conclude that path4 is the dominant reaction path of Fe_1-N_4 catalyst for NH_3-SCR reaction. To further clarify the dominant reaction path of Fe_1-N_4 catalyst for NH_3-SCR reaction, the catalytic cycle of Fe_1-N_4 in the path4 was plotted, as shown in Fig. 4. Obviously, there are two reaction steps, including the interaction between NO_2 and NH_3 as well as the formation of N_2 and $\cdot OH$.

3.4. Thermodynamic analysis

Through the analysis of the above reaction pathways, the detailed reaction pathways, energy profiles and skeletal reaction scheme have been obtained. In addition, thermodynamic analysis is conducted to study the effect of temperature on the NH_3-SCR reaction. The Gibbs free
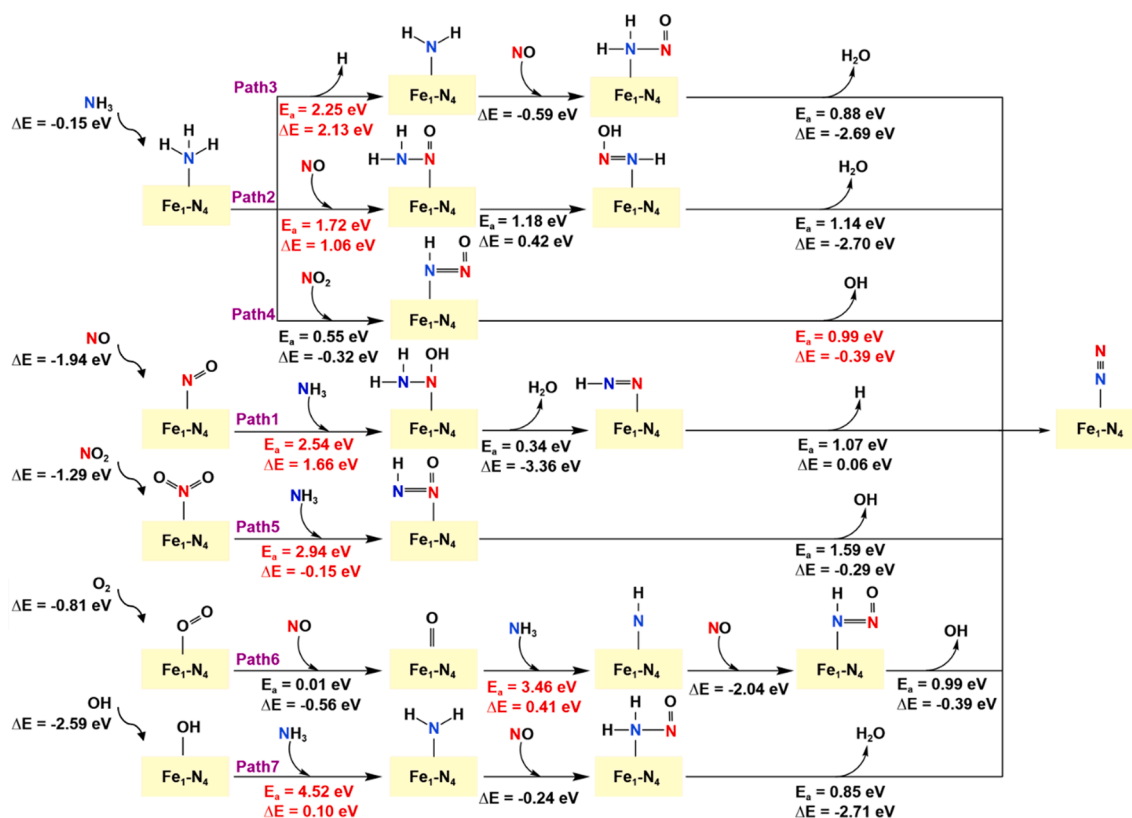
Fig. 3. A skeletal reaction scheme for NH_3-SCR reactions over Fe_1-N_4 catalyst. N atoms of NH_3 and $NO_x(x = 1, 2)$ are highlighted with blue and red, respectively. The rate-determining steps of the reaction are highlighted with red and the activation energy and reaction heat are given in eV. (For interpretation of the references to colour in this figure legend, the reader is referred to the web version of this article.)
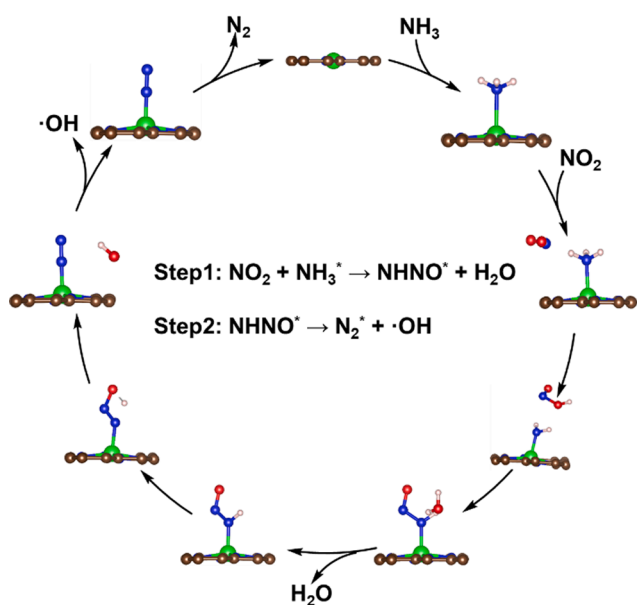

Fig. 4. Catalytic cycle of Fe_1-N_4 in the dominant reaction path for NH_3-SCR (path4).

energy (ΔG) of the eight pathways versus temperature (T) is plotted in Fig. S10. The value of ΔG less than zero indicates that the reaction is spontaneous, and when it is greater than zero, it is non-spontaneous. Apart from path1, the remaining seven pathways are all spontaneous in the temperature range of 298.15–1000 K. To be specific, path3 and

path7 are slightly suppressed by temperature. Fig. 5(a) shows the curve of the natural logarithm of the equilibrium constant (ln$K$) with temperature (T). When the equilibrium constant is greater than 10^5, the reaction is completely irreversible [56]. When the temperature is below 700 K, apart from path1, the remaining pathways are completely irreversible, but when the temperature is above 700 K, path2, path4 and path5 may not be conducted irreversibly and completely. From the above thermodynamic analysis, it can be inferred that path1 is not a dominant reaction. In addition, although path7 is more spontaneous and irreversible, it may not be a main reaction due to its high energy barrier of the RDS (4.52 eV). On the contrary, the moderate Gibbs free energy and reaction equilibrium constant of path4 with its low energy barrier of the RDS (0.99 eV) demonstrate that path4 is the dominant reaction pathway. The more negative Gibbs free energy (ΔG) value and the higher equilibrium constant at low temperature both indicate that the NH_3-SCR over Fe_1-N_4 catalyst is more suitable to occur at low temperature.

3.5. Kinetic analysis

To assess the speed of the NH_3-SCR reaction over Fe_1-N_4 catalyst, kinetic analysis was used to examine the kinetic characteristics of the different reaction pathways. The RDS of the eight reaction pathways were selected as representative for kinetic analysis. According to the traditional transition state theory, the natural logarithm of reaction rate constants (lnk^{TST}) versus temperature (T) can be obtained, as shown in Fig. 5(b). Meanwhile, the activation energy and pre-exponential factor of different reaction pathways are acquired by linearly fitting the reaction rate constants, as listed in Table2. From Fig. 5(b), the reaction rate constants increase with rising temperature, which indicates that increasing temperature can accelerate the NH_3-SCR reaction. Among the different reaction pathways, path4 has the largest reaction rate constant,
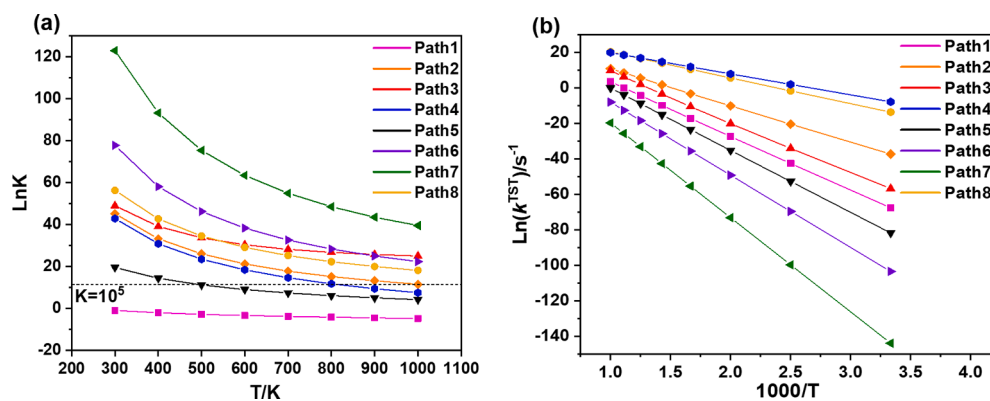
Fig. 5. (a) The logarithm of reaction equilibrium constants of different reaction pathways. (b) The logarithm of reaction rate constants of rate-determining steps.

Table 2
Kinetic parameters for different reaction pathways.

Paths	E_a(eV)	$A(s^{-1})$
path1	2.63	4.78×10^{14}
path2	1.78	4.32×10^{13}
path3	2.45	2.09×10^{16}
path4	1.02	6.21×10^{13}
path5	3.02	1.49×10^{15}
path6	3.52	1.68×10^{14}
path7	4.59	3.43×10^{14}
path8	1.25	1.36×10^{15}

and path7 has the smallest reaction rate constant. Moreover, the lower activation energy of path4 is 1.02 eV, demonstrating that this pathway should be the dominant reaction pathway of NH$_3$-SCR on Fe$_1$-N$_4$ catalyst. Essentially, the NH$_3$-SCR reaction on Fe$_1$-N$_4$ catalyst is not the direct reaction of NO with NH$_3$, but the reduction reaction of NO$_2$ with NH$_3$, which is the most significant difference from traditional catalysts.

3.6. Microkinetic modeling

To further evaluate catalyst activity under flue gas conditions, microkinetic modeling based on above calculated kinetic parameters was conducted by using the CatMAP software [57]. The temperature (T) and logarithm of pressure (log$P$) are selected as two descriptors, and turnover frequency (TOF) values are used as a parameter of reaction rate, as shown in Fig. 6. Simultaneously, the transformation of coverage with the temperature (T) and the logarithm of pressure (log$P$) is plotted in Fig. S4. From Fig. 6, high TOF values are marked with yellow and low TOF values are highlighted in blue. path4 exhibits the highest rate with a wide area in the descriptor space. This is consistent with the previous reaction path, thermodynamic, and kinetic analysis, indicating that path4 is the dominant pathway and the temperature window with Fe$_1$-N$_4$ is 300–430 K. The coverage of NO* and NO$_2$* of path1 and path5 demonstrates that increasing temperature and pressure can accelerate the reaction rate, but the values of TOF are still low ($<10^{-9}$ S^{-1}). Although the NH$_3$* coverage of path2 and path3 is zero, the H* coverage of path2 and the extremely low TOF value in the descriptor space ($<10^{-15}$ S^{-1}) indicate that the reaction has difficulty occurring. On the contrary, the H* coverage of path3 shows that the reaction can occur under high temperature and pressure. The O$_2$* coverage of path6 indicates that NO oxidation is likely promoted, and the high O* coverage is due to the higher adsorption energy of the O atom(-4.5 eV). path7 is unable to react within the descriptor space and requires higher temperature and pressure.

3.7. Activity comparison

According to the above analysis, the dominant pathway of NH$_3$-SCR reaction over Fe$_1$-N$_4$ catalysts includes three steps: (1) NO + O$_2$* → O* + NO$_2$, (2) NO$_2$ + NH$_3$* → NHNO* + H$_2$O, and (3) NHNO* → N$_2$* + ·OH. The RDS is the final step with an energy barrier of 0.99 eV, which is lower than that of the commonly used metal oxides, zeolites, spinels, and metal–organic framework catalysts (as shown in Table 3). The lower energy barrier of the Fe$_1$-N$_4$ catalyst than other SCR catalysts can provide solid evidence that the Fe$_1$-N$_4$ catalyst has super high catalytic activity in NH$_3$-SCR reaction. In addition, the super high catalytic activity of Fe$_1$-N$_4$ catalyst should originate from its unique coordination environment.

4. Conclusions

Based on DFT calculations, the adsorption behavior of various gases (NH$_3$, NO, NO$_2$, O$_2$, ·OH, N$_2$), reaction pathways of NH$_3$-SCR, the influence of temperature on the equilibrium constant (K) and reaction rate constant (k^{TST}), and turnover frequency (TOF) were systematically analyzed. Seven possible reaction pathways were found in NH$_3$-SCR reaction. Different from metal oxides, special intermediates, such as N$_2$H and NHNO exist. The results demonstrate that the dominant pathway of NH$_3$-SCR reaction over Fe$_1$-N$_4$ catalyst is a three-step process including NO oxidation, NO$_2$ reduction, and NHNO decomposition. The energy barrier of rate-determining step is 0.99 eV which is obviously lower than that of other SCR catalysts. Different from other metal oxide catalysts, the fast oxidation of NO on Fe$_1$-N$_4$ catalyst contributes to the reaction of "Fast SCR", which significantly promotes the reaction rate of NH$_3$-SCR reaction on Fe$_1$-N$_4$ catalyst. Additionally, the NH$_3$-SCR reaction over Fe$_1$-N$_4$ catalyst can proceed spontaneously and irreversibly at low temperature with an optimal temperature window of the Fe$_1$-N$_4$ catalyst from 300 to 430 K. According to our theoretical results, Fe$_1$-N$_4$ can be a novel environmentally friendly low-temperature catalyst, which provides new insights for designing novel catalyst for NH$_3$-SCR and fundamental guidance for subsequent experimental research. Inspired by the super high catalytic activity of Fe$_1$-N$_4$ catalyst, the subsequent experimental study will be carried out in the future.

CRediT authorship contribution statement

Weijie Yang: Conceptualization, Resources, Writing - original draft, Writing - review & editing, Funding acquisition. **Jianuo Ren:** Formal analysis, Investigation, Writing - original draft, Writing - review & editing. **Hanwen Zhang:** Validation, Methodology. **Jiajia Li:** Validation, Methodology. **Chongchong Wu:** Writing - original draft, Writing - review & editing. **Ian D. Gates:** Writing - original draft, Writing - review & editing. **Zhengyang Gao:** Supervision.
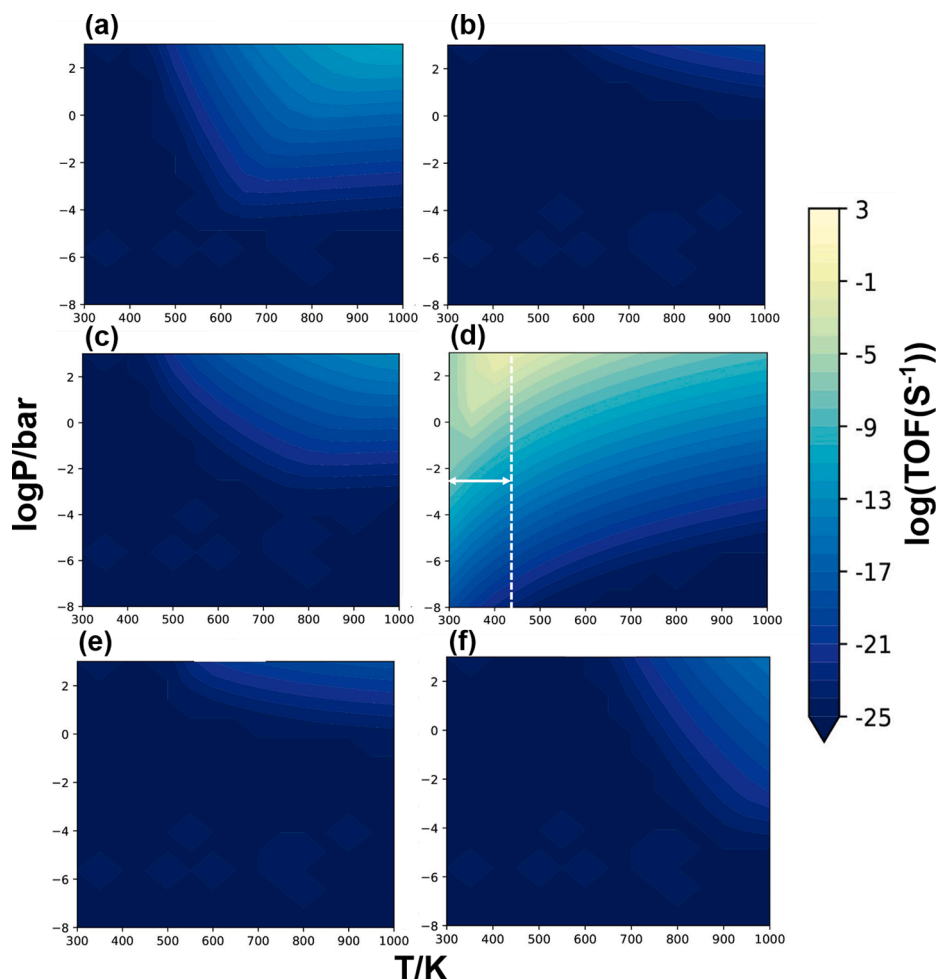
Fig. 6. N$_2$ production rate-temperature/pressure plots for (a) path1 (NH$_3$ + NO* → N$_2$H* + H$_2$O, N$_2$H* → N$_2$* + H*), (b) path2 (NO + NH$_3$* → NH$_2$NO* + H*, NH$_2$NO* →N$_2$* + H$_2$O), (c) path3 (NH$_3$* → NH$_2$* + H*, NH$_2$NO* → N$_2$* + H$_2$O), (d) path4 (NO$_2$ + NH$_3$* → NHNO* + H$_2$O, NHNO* → N$_2$* + ·OH), (e) path5 (NH$_3$ + NO$_2$* → NHNO* + H$_2$O, NHNO* → N$_2$* + ·OH) and (f) path6 (NO + O$_2$* → O* + NO$_2$, NH$_3$ + O* → NH* + H$_2$O, NHNO* → N$_2$* + ·OH).

Table 3
Energy barriers of RDS for NH$_3$-SCR over various catalysts.

Catalyst	Energy barriers of RDS (eV)
V$_2$O$_5$/TiO$_2$	1.36/1.24 [54]
CeO$_2$/TiO$_2$	1.60 [52]
MnO$_x$/TiO$_2$	2.59/3.69 [58]
Mn/γ-Al$_2$O$_3$	1.16/4.72 [59]
Cu^{II}-2Al-*cha*	1.74/1.98 [60]
Cu^{II}OH-Al-*cha*	1.78 [60]
Cu/SAPO-11	2.65 [61]
Cu-SAPO-34	1.50 [62]
NiCr$_2$O$_4$	1.01 [63]
MIL-100-Fe	1.67 [64]
Fe-Exchanged Zeolites	1.04 [65]
Fe–Ni–W Exchanged Zeolites	1.12/1.01 [66]
This work	0.99

Declaration of Competing Interest

The authors declare that they have no known competing financial interests or personal relationships that could have appeared to influence the work reported in this paper.

Acknowledgements

Appendix A. Supplementary data

Supplementary data to this article can be found online at https://doi.org/10.1016/j.fuel.2021.121041.

References

[1] Chen C, Cao Y, Liu S, Chen J, Jia W. Review on the latest developments in modified vanadium-titanium-based SCR catalysts. Chin J Catal 2018;39(8):1347–65.
[2] Zhang R, Liu N, Lei Z, Chen B. Selective transformation of various nitrogen-containing exhaust gases toward N$_2$ over zeolite catalysts. Chem Rev 2016;116(6): 3658–721.
[3] Han L, Cai S, Gao M, Hasegawa J-y, Wang P, Zhang J, et al. Selective catalytic reduction of NO$_x$ with NH$_3$ by using novel catalysts: state of the art and future prospects. Chem Rev 2019;119(19):10916–76.
[4] Liu Y, Zhao J, Lee J-M. Conventional and new materials for selective catalytic reduction (SCR) of NO$_x$. ChemCatChem 2018;10(7):1499–511.
[5] Wang T, Liu H, Zhang X, Guo Y, Zhang Y, Wang Y, et al. A plasma-assisted catalytic system for NO removal over CuCe/ZSM-5 catalysts at ambient temperature. Fuel Process Technol 2017;158:199–205.
[6] Li Yi, Li Y, Wang P, Hu W, Zhang S, Shi Q, et al. Low-temperature selective catalytic reduction of NO$_x$ with NH$_3$ over MnFeO$_x$ nanorods. Chem Eng J 2017;330:213–22.
[7] Wang H, Yuan B, Hao R, Zhao Yi, Wang X. A critical review on the method of simultaneous removal of multi-air-pollutant in flue gas. Chem Eng J 2019;378: 122155. https://doi.org/10.1016/j.cej.2019.122155.

[8] Yuan B, Mao X, Wang Z, Hao R, Zhao Y. Radical-induced oxidation removal of multi-air-pollutant: A critical review. J Hazard Mater 2020;383:121162. https://doi.org/10.1016/j.jhazmat.2019.121162.

[9] Chen L, Weng D, Wang J, Weng D, Cao Li. Low-temperature activity and mechanism of WO₃-modified CeO₂-TiO₂ catalyst under NH₃-NO/NO₂ SCR conditions. Chin J Catal 2018;39(11):1804–15.

[10] Koebel M, Elsener M, Madia G. Reaction pathways in the selective catalytic reduction process with NO and NO₂ at low temperatures. Indus Eng Chem Res 2001;40(1):52–9.

[11] Hong Z, Wang Z, Li X. Catalytic oxidation of nitric oxide (NO) over different catalysts: an overview. Catal Sci Technol 2017;7(16):3440–52.

[12] Zhang S, Zhao Y, Yang J, Zhang Yi, Sun P, Yu X, et al. Simultaneous NO and mercury removal over MnOₓ/TiO₂ catalyst in different atmospheres. Fuel Process Technol 2017;166:282–90.

[13] Husnain N, Wang E, Li K, Anwar MT, Mehmood A, Gul M, et al. Iron oxide-based catalysts for low-temperature selective catalytic reduction of NOx with NH3. Rev Chem Eng 2019;35(2):239–64.

[14] Zhang Y-s, Li C, Yu C, Tran T, Guo F, Yang Y, et al. Synthesis, characterization and activity evaluation of Cu-based catalysts derived from layered double hydroxides (LDHs) for DeNOₓ reaction. Chem Eng J 2017;330:1082–90.

[15] Chen L, Si Z, Wu X, Weng D. DRIFT study of CuO–CeO₂–TiO₂ mixed oxides for NOₓ reduction with NH₃ at Low temperatures. ACS Appl Mater Interfaces 2014;6(11):8134–45.

[16] Yu K, Lou L-L, Liu S, Zhou W. Asymmetric oxygen vacancies: the intrinsic redox active sites in metal oxide catalysts. Adv Sci 2020;7(2):1901970. https://doi.org/10.1002/advs.201901970.

[17] Chen ZW, Chen LX, Yang CC, Jiang Q. Atomic (single, double, and triple atoms) catalysis: frontiers, opportunities, and challenges. J Mater Chem A 2019;7(8):3492–515.

[18] Lin J, Qiao B, Li N, Li L, Sun X, Liu J, et al. Little do more: a highly effective Pt₁/FeOₓ single-atom catalyst for the reduction of NO by H₂. Chem Commun 2015;51(37):7911–4.

[19] Xing F, Jeon J, Toyao T, Shimizu K-I, Furukawa S. A Cu–Pd single-atom alloy catalyst for highly efficient NO reduction. Chem Sci 2019;10(36):8292–8.

[20] Deng D, Chen X, Yu L, Wu X, Liu Q, Liu Y, et al. A single iron site confined in a graphene matrix for the catalytic oxidation of benzene at room temperature. Sci Adv 2015;1(11):e1500462. https://doi.org/10.1126/sciadv.1500462.

[21] Cui X, Li H, Wang Y, Hu Y, Hua L, Li H, et al. Room-temperature methane conversion by graphene-confined single iron atoms. Chem 2018;4(8):1902–10.

[22] Jiao L, Zhang R, Wan G, Yang W, Wan X, Zhou H, et al. Nanocasting SiO₂ into metal-organic frameworks imparts dual protection to high-loading Fe single-atom electrocatalysts. Nat Commun 2020;11(1). https://doi.org/10.1038/s41467-020-16715-6.

[23] Gao Z-Y, Yang W-J, Ding X-L, Lv G, Yan W-P. Support effects on adsorption and catalytic activation of O₂ in single atom iron catalysts with graphene-based substrates. PCCP 2018;20(10):7333–41.

[24] Yang W, Gao Z, Liu X, Li X, Ding X, Yan W. Single-atom iron catalyst with single-vacancy graphene-based substrate as a novel catalyst for NO oxidation: a theoretical study. Catal Sci Technol 2018;8(16):4159–68.

[25] Yang W, Zhao M, Ding X, Ma K, Wu C, Gates ID, et al. The effect of coordination environment on the kinetic and thermodynamic stability of single-atom iron catalysts. PCCP 2020;22(7):3983–9.

[26] Bogojeski M, Vogt-Maranto L, Tuckerman ME, Muller KR, Burke K. Quantum chemical accuracy from density functional approximations via machine learning. Nat Commun 2020;11(1):5223.

[27] Kresse G, Furthmüller J. Efficiency of ab-initio total energy calculations for metals and semiconductors using a plane-wave basis set. Comput Mater Sci 1996;6(1):15–50.

[28] Kresse G, Joubert D. From ultrasoft pseudopotentials to the projector augmented-wave method. Phys Rev B 1999;59(3):1758–75.

[29] Kresse G, Furthmüller J. Efficient iterative schemes for ab initio total-energy calculations using a plane-wave basis set. Phys Rev B 1996;54(16):11169–86.

[30] Monkhorst HJ, Pack JD. Special points for Brillouin-zone integrations. Phys Rev B 1976;13(12):5188–92.

[31] Yan Ge, Gao Z, Zhao M, Ma K, Ding Z, Yang W, et al. Mechanism study on CO₂ reforming of methane over platinum cluster doped graphene: A DFT calculation. Mol Catal 2020;497:111205. https://doi.org/10.1016/j.mcat.2020.111205.

[32] Yan Ge, Gao Z, Zhao M, Yang W, Ding X. CO₂ hydrogenation to formic acid over platinum cluster doped defective graphene: a DFT study. Appl Surf Sci 2020;517:146200. https://doi.org/10.1016/j.apsusc.2020.146200.

[33] Li H, Xu S, Wang M, Chen Z, Ji F, Cheng K, et al. Computational design of (100) alloy surfaces for the hydrogen evolution reaction. 2020;8(35):17987–97.

[34] Vojvodic A, Nørskov JK, Abild-Pedersen F. Electronic structure effects in transition metal surface chemistry. Top Catal 2014;57(1-4):25–32.

[35] Chen P, Gu M, Chen X, Chen J. Study of the reaction mechanism of oxygen to heterogeneous reduction of NO by char. Fuel 2019;236:1213–25.

[36] Yang W, Li L, Zhao M, Huang H, Ding X, Wu C, et al. Theoretical prediction of graphene-based single-atom iron as a novel catalyst for catalytic oxidation of Hg⁰ by O₂. Appl Surf Sci 2020;508:145035. https://doi.org/10.1016/j.apsusc.2019.145035.

[37] Henkelman G, Jónsson H. Improved tangent estimate in the nudged elastic band method for finding minimum energy paths and saddle points. J Chem Phys 2000;113(22):9978–85.

[38] Henkelman G, Uberuaga BP, Jónsson H. A climbing image nudged elastic band method for finding saddle points and minimum energy paths. J Chem Phys 2000;113(22):9901–4.

[39] Chen P, Gu M, Wang D, Wang J, Huang X, Wang H, et al. Experimental and density functional theory study of the influence mechanism of oxygen on NO heterogeneous reduction in deep air-staged combustion. Combustion Flame 2021;223:127–41.

[40] Heyden A, Bell AT, Keil FJ. Efficient methods for finding transition states in chemical reactions: comparison of improved dimer method and partitioned rational function optimization method. J Chem Phys 2005;123(22):224101. https://doi.org/10.1063/1.2104507.

[41] Yang W, Gao Z, Liu X, Ma C, Ding X, Yan W. Directly catalytic reduction of NO without NH₃ by single atom iron catalyst: A DFT calculation. Fuel 2019;243:262–70.

[42] Riplinger C, Carter EA. Cooperative effects in water binding to cuprous oxide surfaces. J Phys Chem C 2015;119(17):9311–23.

[43] Bendavid LI, Carter EA. CO₂ adsorption on Cu₂O (111): a DFT+ U and DFT-D study. J Phys Chem C 2013;117(49):26048–59.

[44] Gao Z, Yang W, Ding Z, Ding Yi, Yan W. Theoretical research on heterogeneous reduction of N₂O by char. Appl Therm Eng 2017;126:28–36.

[45] Gao Z, Yang W, Ding X, Lv G, Yan W. Support effects in single atom iron catalysts on adsorption characteristics of toxic gases (NO₂, NH₃, SO₃ and H₂S). Appl Surf Sci 2018;436:585–95.

[46] Wang J, Deng S, Liu Z, Liu Z. The rare two-dimensional materials with Dirac cones. Natl Sci Rev 2015;2(1):22–39.

[47] Pan Y, Chen Y, Wu K, Chen Z, Liu S, Cao X, et al. Regulating the coordination structure of single-atom Fe-NₓCᵧ catalytic sites for benzene oxidation. Nat Commun 2019;10(1). https://doi.org/10.1038/s41467-019-12362-8.

[48] Zhu Y, Sun W, Luo J, Chen W, Cao T, Zheng L, et al. A cocoon silk chemistry strategy to ultrathin N-doped carbon nanosheet with metal single-site catalysts. Nat Commun 2018;9(1). https://doi.org/10.1038/s41467-018-06296-w.

[49] Zhao Lu, Zhang Y, Huang L-B, Liu X-Z, Zhang Q-H, He C, et al. Cascade anchoring strategy for general mass production of high-loading single-atomic metal-nitrogen catalysts. Nat Commun 2019;10(1). https://doi.org/10.1038/s41467-019-09290-y.

[50] Janthon P, Kozlov SM, Viñes F, Limtrakul J, Illas F. Establishing the accuracy of broadly used density functionals in describing bulk properties of transition metals. J Chem Theory Comput 2013;9(3):1631–40.

[51] Yang Y, Liu J, Wang Z, Liu F. A skeletal reaction scheme for selective catalytic reduction of NOₓ with NH₃ over CeO₂/TiO₂ catalyst. Fuel Process Technol 2018;174:17–25.

[52] Yang Y, Liu J, Liu F, Wang Z, Ding J, Huang H. Reaction mechanism for NH₃-SCR of NOₓ over CuMn₂O₄ catalyst. Chem Eng J 2019;361:578–87.

[53] Liu Z, Zhang S, Li J, Ma L. Promoting effect of MoO₃ on the NOₓ reduction by NH₃ over CeO₂/TiO₂ catalyst studied with in situ DRIFTS. Appl Catal B 2014;144:90–5.

[54] He G, Lian Z, Yu Y, Yang Y, Liu K, Shi X, et al. Polymeric vanadyl species determine the low-temperature activity of V-based catalysts for the SCR of NOx with NH3. Sci Adv 2018;4(11):eaau4637.

[55] Zheng H, Song W, Zhou Y, Ma S, Deng J, Li Y, et al. Mechanistic study of selective catalytic reduction of NOₓ with NH₃ over Mn-TiO₂: a combination of experimental and DFT study. J Phys Chem C 2017;121(36):19859–71.

[56] Yang W, Gao Z, Liu X, Ding X, Yan W. The adsorption characteristics of As₂O₃, Pb⁰, PbO and PbCl₂ on single atom iron adsorbent with graphene-based substrates. Chem Eng J 2019;361:304–13.

[57] Medford AJ, Shi C, Hoffmann MJ, Lausche AC, Fitzgibbon SR, Bligaard T, et al. CatMAP: a software package for descriptor-based microkinetic mapping of catalytic trends. Catal Lett 2015;145(3):794–807.

[58] Wei Lu, Cui S, Guo H, Ma X. Study on the role of Mn species in low temperature SCR on MnOₓ/TiO₂ through experiment and DFT calculation. Mol Catal 2018;445:102–10.

[59] Li X, Li Q, Zhong L, Song Z, Yu S, Zhang C, et al. DFT analysis of the reaction mechanism for NH₃-SCR of NOₓ over Mn/γ-Al₂O₃ catalyst. J Phys Chem C 2019;123(41):25185–96.

[60] Zhao P, Boekfa B, Shimizu K-I, Ogura M, Ehara M. Selective catalytic reduction of NO with NH₃ over Cu-exchanged CHA, GME, and AFX zeolites: a density functional theory study. Catalysis. Sci Technol 2021;11(5):1780–90.

[61] Griffe B, Brito JL, Sierraalta A. Selective catalytic reduction of nitrogen oxide by ammonia over Cu/SAPO-11: a theoretical study. SN Appl Sci 2020;2(7):1–13.

[62] Yang G, Ran J, Du X, Wang X, Chen Y, Zhang L. Different copper species as active sites for NH₃-SCR reaction over Cu-SAPO-34 catalyst and reaction pathways: a periodic DFT study. Microporous Mesoporous Mater 2018;266:223–31.

[63] Shen S, Liu Yi, Zhai D, Qian G. Electroplating sludge-derived spinel catalysts for NO removal via NH₃ selective catalysis reduction. Appl Surf Sci 2020;528:146969. https://doi.org/10.1016/j.apsusc.2020.146969.

[64] Zhang M, Wang W, Chen Y. Theoretical investigation of selective catalytic reduction of NO on MIL-100-Fe. PCCP 2018;20(4):2211–9.

[65] Li J, Li S. A DFT study toward understanding the high activity of Fe-exchanged zeolites for the "fast" selective catalytic reduction of nitrogen oxides with ammonia. J Phys Chem C 2008;112(43):16938–44.

[66] Liu H, You C, Wang H. Experimental and density functional theory studies on the zeolite-based Fe–Ni–W trimetallic catalyst for high-temperature NOₓ selective catalytic reduction: identification of active sites suppressing ammonia over-oxidation. ACS Catal 2021;11(3):1189–201.